Possible role of grain-boundary and dislocation structure for the magnetic-flux trapping behavior of niobium: A first-principles study

P. Garg,[1] C. Muhich,[1] L. D. Cooley,[2] T. R. Bieler,[3] and K. N. Solanki[1,*]

[1]*School for Engineering of Matter, Transport, and Energy, Arizona State University, Tempe, Arizona 85287, USA*
[2]*The Applied Superconductivity Center, National High Magnetic Field Laboratory, Tallahassee, Florida 32310, USA*
[3]*Department of Material Sciences and Engineering, Michigan State University, East Lansing, Michigan 48824, USA*

(Received 9 December 2019; revised manuscript received 14 February 2020; accepted 14 April 2020; published 6 May 2020)

First-principles methods were used to understand magnetic flux trapping at vacancies, dislocations, and grain boundaries in high-purity superconducting niobium. Full-potential linear augmented plane-wave methods were applied in progressively greater complexity, starting at simple vacancies and extending to screw dislocations and tilt grain boundaries to analyze the effects of magnetic field on the superconducting state surrounding these defects. Density-functional theory calculations identified changes in electronic structure at the dislocation core and different types of symmetric tilt grain boundaries relative to bulk niobium. Electron redistribution enhanced nonparamagnetic effects and thus perturb superconductivity, resulting in local conditions suitable for premature flux penetration and subsequently flux pinning. Since the coherence length of superconducting niobium at 0 K is significantly larger than the lattice parameter, the effects of line and planar defects in niobium are predicted to be stronger for defect clusters than single defects in isolation, which is consistent with recent experimental observations. Controlling accumulation or depletion of charge at the defects, e.g., by segregation of an impurity atom, can mitigate these tendencies thus increasing the quality of superconducting niobium.

DOI: 10.1103/PhysRevB.101.184102

I. INTRODUCTION

Niobium is a central material to superconductivity. Alloyed forms of niobium are used in magnetic superconductors for magnetic resonance imaging and nuclear magnetic resonance instruments in medical diagnostics [1,2]. Pure niobium is also used in many applications to fabricate superconducting radio frequency (SRF) cavities; improvements in technology have improved the performance in accelerating charged particle beams, especially when high power and high energy is required to develop high-performance particle accelerators [3,4]. Niobium is also used for making superconducting quantum interference devices (SQUID) used in superconducting electronics and microelectronics and more recently in quantum information and communications technology [5–7]. For the above applications of niobium, defect and surface engineering is important because material imperfections such as defects, impurities, etc. adversely affect the superconductivity of niobium.

Superconducting niobium operates in the Meissner state such that the external magnetic field is completely expelled from the superconductor [8]. However, lattice defects including dislocations, grain boundaries and impurities such as hydrogen that generate hydride precipitates, etc. suppress the expulsion of magnetic field and pin the field inside the material even after the external magnetic field is removed [9,10]. The trapped field is present in the form of quantized vortices which have a normal conducting core, where unpaired electrons cause Ohmic resistance that decreases the niobium superconductivity [11]. SRF and SQUID applications cannot tolerate losses due to moving flux, so the applications require a flux-free state. Thus, electronic devices and SRF cavities are carefully cooled to the superconducting state in zero field by shielding the devices from the Earth's magnetic field. Control of growth orientation and defect structures was identified long ago as an important requirement for niobium single-vortex devices, which underpin many applications in quantum logic and astrophysics [12,13]. SQUIDs and small devices are shielded and flux trapping is not a major issue since these devices are engineered to not allow flux lines to penetrate by making traces thinner than the penetration depth. However it is practically impossible to shield SRF cavities, with over 1 square meter of area, from the background fields such that no flux lines will be present at all.

In SRF cavities, electromagnetic fields are used accelerate charged particles towards a desired target; however if a magnetic field is trapped in the cavity there are significant power losses. The performance of SRF cavities is measured in terms of the quality factor $Q_O = G/R_S$, where the geometric factor G depends on the cavity geometry and R_S is the surface resistance of the inner cavity wall [14,15]. The surface resistance (R_S) defines the power dissipation at the inner surface of SRF cavity and is comprised of two terms: the Bardeen-Cooper-Schrieffer (BCS) resistance R_{BCS} and the residual surface resistance R_{res} [16,17]. The R_{BCS} term originates from microwave absorption by thermally excited quasiparticles and becomes zero as $T \to 0$ because

*Corresponding author: kiran.solanki@asu.edu

quasiparticle excitation ceases at 0 K [18]. In contrast, R_{res} remains finite as $T \rightarrow 0$ and arises from magnetic flux trapping, normal conducting precipitates, impurities, defects etc., which depend on the material properties [19,20]. The major contribution to R_{res} stems from magnetic flux trapping at defects during cavity cooling [21,22] and therefore it is critical to reduce the trapped magnetic flux in order to improve Q_O of niobium SRF cavities. Increase in R_{res} also degrades the quality of niobium for microwave oscillators and superconducting resonators for quantum information processing with solid-state qubit devices. Thus, flux trapping at the crystal lattice imperfections such as dislocations and grain boundaries contribute to R_{res} and significantly degrade the performance of niobium for various superconducting applications [23–26].

In 1968, Gifkins *et al.* [27] measured flux pinning at grain boundaries of a type II superconductor from the average remnant induction obtained after removal of the applied field and found that it varies with the grain size. Flux pinning at niobium grain boundaries depended on the grain boundary tilt axis [28] and was attributed to the local change in the Ginzburg-Landau free energy [29] and the electron-scattering mechanism [30]. Grain boundaries extend over few atomic layers and act as strong flux pinning centers in high temperature superconductors or superconductors with small coherence lengths such as Nb_3Sn [31]. Although grain boundaries are regions with weakened superconductivity several experiments show that grain boundaries are not strong flux pinning centers in niobium due to its much larger coherence length ($\sim$40 nm) as compared to the grain boundary region [32–34]. However, most superconductors allow flux to slide along the grain boundaries and experience pinning at the planar defects which decreases the critical current density and negatively affects the superconductivity of material [35,36]. Weakening of superconductivity at the grain boundary may lead to premature flux penetration along the grain boundary as observed during magneto-optical imaging of cold worked niobium bicrystal [26,37]. A nonuniform distribution of dislocations was also observed to interact with and trap flux lines in cold rolled polycrystalline niobium [38]. Nearly 100% flux trapping was reported in polycrystalline niobium which reduced to $\sim$41% in heat treated and polished single-crystal niobium samples [11]. Flux trapping due to hydride segregation along the low angle grain boundaries has also been reported during magneto-optical imaging analysis [39]. Recent work by Wang *et al.* shows clear evidence for enhanced flux penetration along both low- and high-angle grain boundaries in Nb [40]. But the large coherence length of niobium makes the models described above not plausible—the boundary should have a negligible effect, which raises the question as to what is causing the grain boundaries to be less than fully superconducting as compared to the bulk.

In general, the pinning mechanism of defects for a given superconducting material can be classified into the condensation energy interaction, the elastic interaction, the magnetic interaction and the kinetic energy interaction [31,41,42]. Several theories such as crystal anisotropy of the upper critical field [29,43,44], electron-scattering at the grain boundary [30], and elastic interactions between the dislocations present at the grain boundaries and the flux line lattice [45] have been proposed to explain flux trapping at defects. However, the mechanism underlying the flux pinning/penetration at defects has not been unequivocally established since the applicability of various flux pinning theories at defects has not been determined for a wide variety of samples.

This work provides a first attempt to understand the interactions between external magnetic field and lattice defects, i.e., vacancies, dislocations and grain boundaries in niobium within the first-principles framework. Equilibrium structures for different defects were obtained using molecular dynamics and density functional theory calculations. The external magnetic field was simulated using the all-electron full-potential linearized augmented plane wave code to analyze the interaction between the magnetic field and different lattice defects. The results demonstrate a significant amount of residual flux at different defects in niobium due to the weakening of superconductivity at the defects. Further, grain boundary character was found to play a significant role on the flux penetration behavior since the residual flux was observed to vary with the grain boundary structure (e.g., misorientation angle). To determine the mechanisms underlying the interactions between an external magnetic field and different defects, the electronic structure of defects was analyzed using electronic density of states and Bader charge analysis within the first-principles framework. Changes in the electronic structure of defects as compared to perfect body centered cubic niobium indicates a nonparamagnetic state in the presence of an external magnetic field thereby promoting flux penetration at defects in niobium. Understanding the role of defects on early flux penetration or flux pinning will provide guidance for improving the processing techniques for cavity fabrication that minimize the undesirable defect density, and therefore increase the quality factor of niobium SRF cavities.

II. COMPUTATIONAL METHODOLOGY

The first-principles calculations were performed within the density functional theory (DFT) framework using the Vienna *ab initio* simulation package (VASP) [46,47], with Perdew-Burke-Ernzerhof (PBE) [48,49] exchange-correlation functional. The semicore projector augmented wave (PAW) pseudopotentials were used to represent niobium, explicitly considering the valence 5*s*, 4*d*, and 4*p* electrons. A plane wave basis set with an energy cutoff of 550 eV was used to represent the wave function on a Monkhorst Pack *k*-point mesh, selected after extensive convergence studies for different defect structures [50]. The computed lattice parameter of niobium is 3.31 Å, which was found to match very well with the previously reported experimental value of 3.30 Å and theoretical value of 3.32 Å [23,51].

A. Point defects

A supercell approach was used to model a metal vacancy in a bulk crystal to determine the parameters relevant for vacancy formation. A niobium atom was removed from its lattice site in a $2 \times 2 \times 2$ body centered cubic (bcc) niobium supercell (16 niobium atoms) to represent a vacancy concentration of 6.25 at% and calculate the vacancy formation energy. The *k* point mesh of $13 \times 13 \times 13$ was selected based on convergence studies and the atoms were relaxed with a

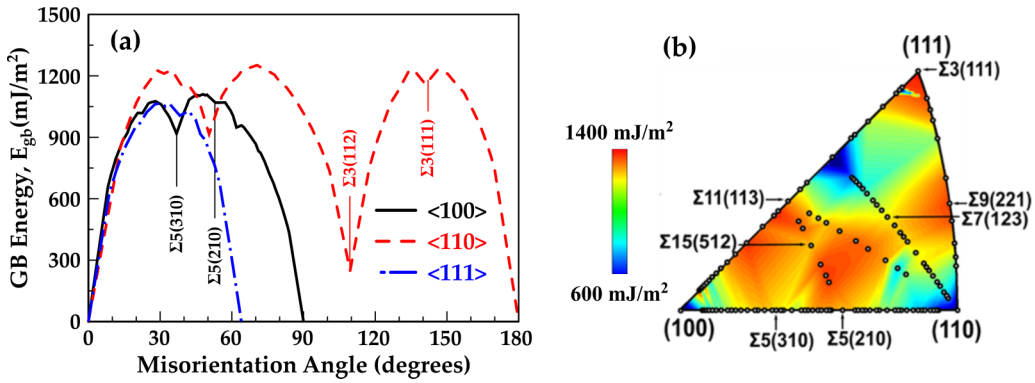

FIG. 1. Grain boundary energy (E_{gb}) represented as a function of (a) misorientation angle and (b) polar and azimuthal angles for ⟨100⟩, ⟨110⟩, and ⟨111⟩ STGBs in Nb. Grain boundaries with low energy are blue regions identified within the standard stereographic triangle.

force and energy convergence criteria of 0.01 eV Å^{-1} and 10^{-6} eV, respectively. The atoms were allowed to relax in all directions to relax the supercell volume and shape. The vacancy formation energy (ΔE_{vac}) is calculated using

$$\Delta E_{vac} = E_{(n-1)} - \frac{n-1}{n} E_n, \tag{1}$$

where E_{n-1} denotes the total energy of the cell containing a vacancy, n is the number of atoms in the supercell and E_n represents the total energy of the perfect supercell without any vacancy [52,53]. The interactions between the vacancies across the periodic boundaries were minimized since the vacancy formation energy for 16 and 24 atom niobium supercells converged within 0.02 eV. The calculated vacancy formation energy value of 2.51 eV was found to be in good agreement with the reported experimental and theoretical values [54,55] that range from 2.32–2.92 eV.

B. Line defects

The screw dislocation dipole structure with 135 atoms in the supercell and a quadrupolar arrangement was created using Stroh's anisotropic field and the elastic constants of niobium [56,57]. The supercell vectors ($\vec{c}_1$, $\vec{c}_2$, $\vec{c}_3$) were selected to accommodate the plastic strain induced by the dislocation dipole and to minimize the elastic energy of the simulation cell. They can be obtained from the unit cell vectors as:

$$\begin{aligned} \vec{c}_1 &= n\vec{a}_1 - q\vec{a}_3, \\ \vec{c}_2 &= \frac{n}{2}\vec{a}_1 + m\vec{a}_2 + \left(\frac{1}{2} - \frac{q}{2}\right)\vec{a}_3, \\ \vec{c}_3 &= \vec{a}_3, \end{aligned} \tag{2}$$

where $\vec{a}_1 = 1/3\ [\bar{1}\bar{1}2]$, $\vec{a}_2 = 1/2\ [1\bar{1}0]$, $\vec{a}_3 = 1/2\ [111]$, $(n, m) = (15, 9)$ for a 135 atom supercell and $q = -1/3\,m$ [58]. The dislocation dipole structure was relaxed using VASP with energy convergence of 10^{-5} eV and 0.01 eV Å^{-1} force tolerance. The atoms were allowed to relax while maintaining a constant volume with a k point grid of $1 \times 1 \times 16$, selected after convergence studies, to minimize the energy of the dislocation dipole. The obtained dislocation core energy of 0.2 eV/b, where b is the Burgers vector on a (110) plane in bcc niobium, matches very well with the values (0.2 eV/b) reported in literature [58].

C. Planar defects

The equilibrium grain boundary (GB) structures were modeled using empirical interatomic potentials in molecular dynamics (MD) simulations. Three symmetric tilt grain boundary (STGB) systems (⟨100⟩, ⟨110⟩, and ⟨111⟩) and a nonsymmetric tilt grain boundary sample were created in Large-scale atomic/molecular massively parallel simulator (LAMMPS) [59] and a semiempirical embedded atom method (EAM) potential for niobium was used [60]. The equilibrium grain boundary structures were determined using a bicrystal simulation cell with 3D periodic boundary conditions and sufficiently large grain interiors perpendicular to the grain boundary to obtain minimum energy GB structures [see Fig. 1(a)] [61–63]. For instance, the Σ5(210) grain boundary was modeled by two (210) oriented slabs of Nb each, reflected with respect to the $x-z$ plane followed by an atom deletion technique and energy minimization using a nonlinear conjugate gradient method [see Fig. 1(b)] [64–66]. All atoms of the GB supercells were allowed to relax to an energy convergence of $<10^{-6}$ eV [67]. The grain boundary energy (E_{gb}) was calculated as the difference between the energy of the GB simulation cell with n atoms (E_n) and the cohesive energy of niobium atoms (E_{coh}) per unit area of the grain boundary plane (A).

$$E_{gb} = \frac{E_n - n * E_{coh}}{2A}. \tag{3}$$

The expression is divided by 2 due to the two interfaces in the grain boundary simulation cell. The GB energy as a function of the misorientation angle for ⟨100⟩, ⟨110⟩, and ⟨111⟩ tilt axes of niobium is shown in Fig. 2(a). Furthermore, Fig. 1(d) shows the variation of grain boundary energy with misorientation angle mapped onto a stereographic triangle with the convention for representing cubic metals. The vertices of the triangle represent the three principal orientations of the cubic system. The GB misorientation is defined by the polar/azimuthal angles and the GB energy is represented by the color contour. The color bar corresponds to the GB energies between 600 and 1400 mJ/m^2, which represents the GB database for the three symmetric tilt axes. The observed trends of the grain boundary energy with misorientation angle are comparable to the previously reported values [68].

Due to the size constraints of first-principles methods, smaller supercells with one periodic length along the GB

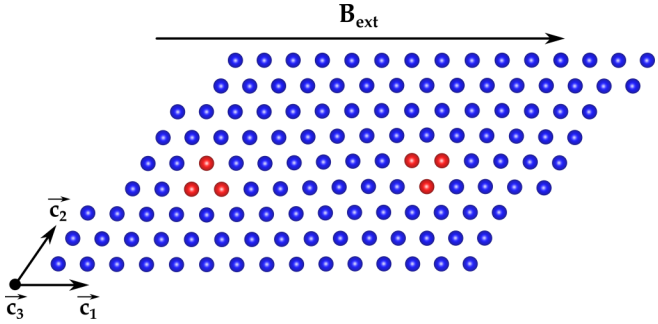

FIG. 2. Screw dislocation core structure on (111) plane in bcc niobium. The atoms are colored according to common neighbor analysis such that dislocation core atoms are red and bcc atoms are blue. The red atoms of the upward and downward triangles in the (111) plane represent the dislocation dipoles with opposite burgers vector. The remnant flux following removal of the magnetic field was 4.70 mT.

and few atomic planes (25–35 atomic planes) perpendicular to the GB plane were obtained from the bicrystal simulation cell of MD calculations. The smaller supercells for different grain boundaries were relaxed within DFT framework. The k-point mesh for each of the GB supercells was selected, after extensive k-point convergence studies (see Table II) and the atoms were relaxed with 10^{-6}-eV energy tolerance while maintaining a constant volume and shape of the supercells. The GB supercells with negligible grain boundary interactions across the periodic images were selected for further studies.

D. External magnetic field

The state-of the-art all-electron full-potential linearized augmented plane wave (FP-LAPW) code was used to analyze the interactions between defects and an external magnetic field [69,70]. The FP-LAPW code formulation is based on the Kohn-Sham equations for external field in a two-step variational process [69,71,72]. In the first-variational step a Hamiltonian ($\hat{H}$) containing only the scalar potential and **E** field is constructed

$$\hat{H} = \hat{T}_s + \hat{V}_{\text{ext}} + \boldsymbol{E}\cdot\hat{\boldsymbol{r}} + \hat{V}_{\text{xc}} \tag{4}$$

and diagonalized with $\hat{H}|\phi_i\rangle = \varepsilon_i|\phi_i\rangle$. $\hat{T}_s$ is the kinetic energy operator, $\hat{V}_{\text{ext}}$ is the external potential operator, $\hat{V}_{\text{xc}}$ is the exchange-correlation (XC) potential operator, and ε_i is the orbital energy of the corresponding Kohn-Sham orbital, ϕ_i [69]. In the second-variational step, the magnetic fields, spin-orbit coupling, and electric field (**A**) are added using the first-variational step as a basis:

$$H_{ij} = \varepsilon_i\delta_{ij} + \langle\phi_i|\boldsymbol{\sigma}\cdot(\hat{\boldsymbol{B}}_{\text{ext}} + \hat{\boldsymbol{B}}_{\text{xc}}) + \boldsymbol{\sigma}\cdot\hat{L} + \boldsymbol{A}\cdot\hat{\nabla}|\phi_i\rangle, \tag{5}$$

where $\boldsymbol{B}_{\text{xc}}$ is the exchange-correlation magnetic field, $\boldsymbol{\sigma}$ is the vector of Pauli matrices, and L is the orbital magnetic moment. Instead of the usual approach of separating the Kohn-Sham equations into spin-up and spin-down orbitals, densities and potentials, the FP-LAPW code formulation treats magnetism as noncollinear for which the basic variables are the scalar density ρ(r) and the magnetization vector field m(r).

An external magnetic field ($B_{\text{ext}} = 171.5$ mT) was applied along different defects below the superconducting transition temperature of niobium ($T_c = 9.25$ K). Niobium is paramagnetic in nature below T_c within the FP-LAPW code formulation. Periodic boundary conditions were maintained along all directions. The magnetic field was reduced by a factor of 0.85 after each ionic step such that the applied field is infinitesimal, i.e., effectively zero at the end of all the steps. The augmented plane wave basis was used to accurately compute the effective potential under the external magnetic field without local discontinuities in the XC potentials introduced by functional approximations. The Fermi-Dirac smearing method with a smearing width of 10^{-4} eV was used for a smooth approximation of the Dirac delta function needed to compute the occupancies of the Kohn-Sham states. The self-consistent loop is converged when the total energy is smaller than 10^{-3} eV and the root mean square change in Kohn-Sham potential and magnetic field is smaller than 10^{-3} T.

III. RESIDUAL FLUX AT DEFECTS

The first step towards understanding the interactions between the magnetic field and different defects is to determine the effect of external magnetic field on pure single crystal niobium. It is very well known that niobium is paramagnetic above its superconducting transition temperature and superconducting below T_c. Hence, there is no flux trapping in niobium and the externally applied magnetic field is completely expelled from the material. This is observed in our FP-LAPW simulations because all spins are evenly distributed through the cell independent of the application of an external field. Next, we examined the effect of point defects, line defects and planar defects on residual flux density.

To examine the role of point defects, the external magnetic field was applied perpendicular to a (100) plane of niobium supercell with a vacancy concentration of 6.25 at%. A very small remnant magnetic moment of 0.005 μ_B was observed in the bcc supercell with 6.25 at% of vacancy after the external magnetic field was reduced to zero. The magnitude of remnant magnetic moment was independent of the direction of applied field due to symmetry. The residual magnetic flux density (B_r) due to different defects was calculated from the remnant magnetic moment (M) as

$$B_r = \frac{M\mu_0}{V}, \tag{6}$$

where V is the volume of supercell in m^3 and μ_0 is the permeability of vacuum ($4\pi \times 10^{-7}$ H/m), which provides a lower bound; the trapped flux could be higher if the volume of the defect was used. Thus, the residual flux density was found to be 0.19 mT for the niobium supercell with a point defect concentration of 6.25 at%. Further, the effect of line defects on residual magnetic flux density in niobium was investigated using the screw dislocation dipole structure. The external magnetic field was applied along $\vec{c}_1$ direction of the supercell and reduced to zero after multiple ionic steps. A remnant magnetic moment of 1.00 μ_B, resulting in 4.70 mT of residual flux density using Eq. (6) was observed in the dislocation dipole structure with supercell volume 2481.2 Å^3.

The role of planar defects on residual magnetic field in niobium was investigated by applying the magnetic field along the GB plane parallel to the x-axis of the simulation cell, as

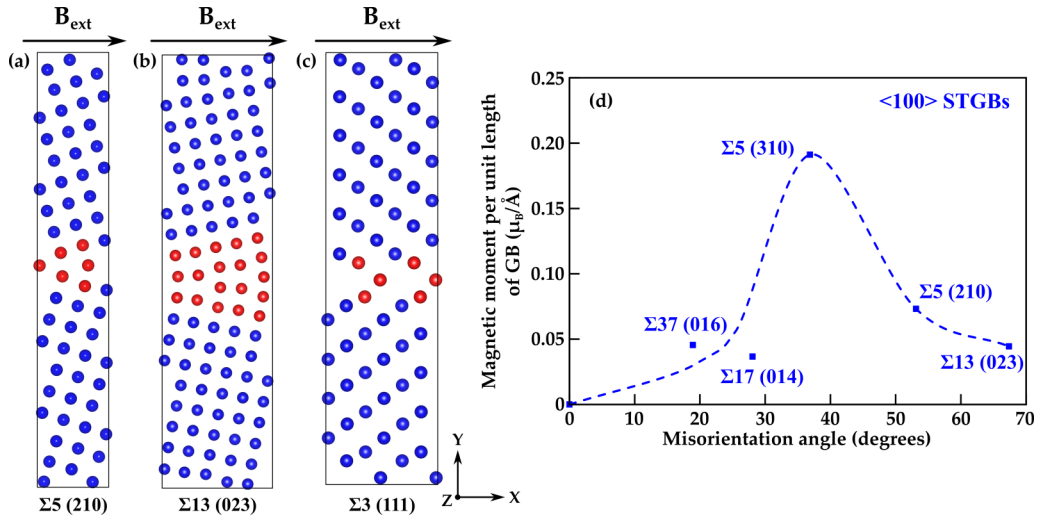

FIG. 3. An external magnetic field ($\boldsymbol{B}_{\text{ext}}$) was applied along the grain boundary plane of (c) Σ5 (210), (d) Σ13 (023), and (e) Σ3 (111) grain boundaries in Nb. (d) The remnant magnetic moment per unit periodic length of GB peaks near 40° GB misorientation for ⟨100⟩ symmetric tilt grain boundaries. Blue and red colored solid circles represent body-centered cubic and grain boundary atomic structures, respectively, obtained from the common neighbor analysis in Ovito.

illustrated in Fig. 3. The applied field was gradually reduced to zero at the end of all self-consistent loops and a residual magnetic moment was observed in the GB simulation cells. For instance, a residual magnetic moment of 0.54 μ_B was observed in the Σ5 (210) grain boundary which corresponds to a 5.74 mT residual field. The magnitude of the residual field was calculated for multiple GB's and the results are reported in Table I. Among different GBs studied here, the residual flux density was minimum for the highly symmetric Σ1 (101) grain boundary ($\theta = 60^\circ$) and the remaining maximum flux was for the Σ3 (111) grain boundary ($\theta = 70.53^\circ$). The grain boundary character was found to play a significant role on the residual flux density behavior of grain boundaries. The remnant magnetic moment per unit periodic length of the GB increased with increasing GB misorientation angle approximately up to $\theta = 40^\circ$ for GBs in the ⟨100⟩ STGB system. However, above 40° the magnetic moment per unit periodic length of the GB decreased gradually, as shown in Fig. 3. The energy difference between the equilibrium grain boundary structure, and the metastable state with trapped flux was found to vary from −1 to −34 meV for different grain boundaries (see Table I).

Next, the Voronoi tessellation method [73] was used to construct a polycrystalline sample of niobium containing grains of identical shape and size with [110] tilt axis to study the residual flux density behavior of a nonsymmetric tilt grain boundary [Fig. 4(a)] [74,75]. The sample was relaxed, within LAMMPS framework, to uniformly distribute the excess free energy in the whole system while maintaining periodic boundary conditions. One of the nonsymmetric tilt grain boundary [as shown in Fig. 4(b)] was translated into first-principles framework using a bicrystal simulation cell with one periodic length along GB owing to the size limitations of first-principles method. The bicrystal simulation cell was relaxed using DFT methods and further examined for residual flux density studies. The magnetic field was applied along x axis, parallel to the GB plane [Fig. 4(b)] and gradually reduced to zero at the end of self-consistent loops. A residual magnetic moment of 0.5 μ_B was observed corresponding to 2.5 mT of residual flux at the [110] nonsymmetric tilt grain boundary.

Overall, the magnitude of the residual field at different grain boundaries was found to vary from 2 to 20 mT. These results are in good agreement with the cold rolled niobium

TABLE I. The magnitude of residual magnetic field and the energy difference for different grain boundaries in niobium.

Residual field at Nb grain boundary					
Grain boundary	Misorientation angle	Volume (Å^3)	Magnetic moment (μ_B)	Residual field (mT)	Energy difference (meV)
Σ5 (210)	53.13°	1098.5	0.54	5.74	−15.15
Σ5 (310)	36.87°	1535.9	2.00	15.17	−14.08
Σ13 (023)	67.38°	1899.2	0.53	3.25	−4.60
Σ37 (016)	18.92°	2633.3	0.92	4.06	−34.1
Σ17 (014)	28.07°	1251.2	0.50	4.66	−1.07
Σ3 (111)	70.53°	1202.8	2.00	19.38	−5.77
Σ1 (101)	60°	1308.9	0.22	1.98	−0.42

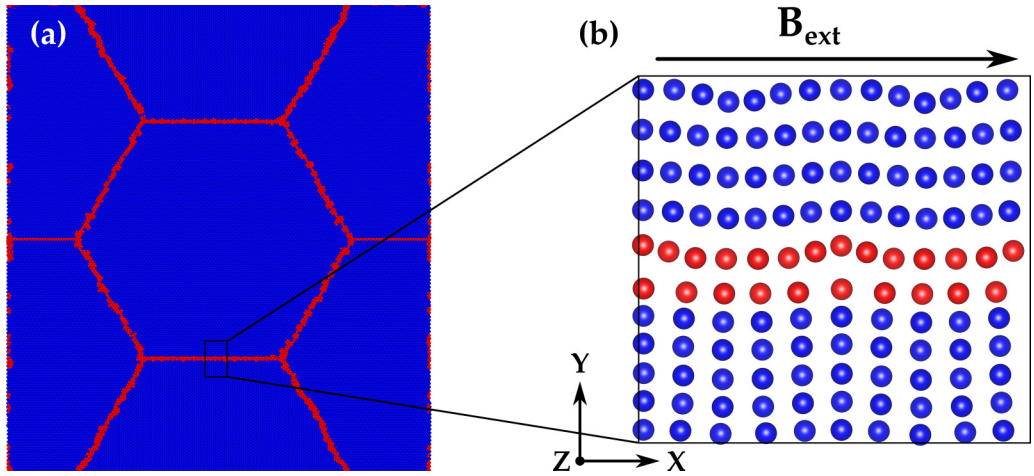

FIG. 4. (a) An equilibrated polycrystalline sample constructed using the Voronoi tessellation consisting of nonsymmetric tilt grain boundaries and (b) schematic of externally applied magnetic field ($\boldsymbol{B}_{ext}$) along the grain boundary plane of a nonsymmetric tilt grain boundary in Nb. Blue and red colored solid circles represent body-centered cubic and grain boundary atomic structures, respectively, obtained from the common neighbor analysis. The z axis is aligned along the [110] direction. This boundary showed a 2.5-mT residual flux.

bicrystal samples where 8 to 20 mT of premature flux penetration was observed along the grain boundaries [26]. The screw dislocation dipole is similar to the boundaries with low flux penetration (4.7 mT), and the vacancy is much smaller (0.19 mT). Although grain boundaries do not strongly affect the SRF behavior of cavities, early field penetration in the grain boundaries when exposed to magnetic fields can be attributed to the disrupted superconductivity at the defects. It is highly probable that these phenomena co-exist and contribute to degraded SRF performance of niobium.

IV. ELECTRONIC STRUCTURE ANALYSIS

An external magnetic field generally interacts with both the electron spin and the electronic orbital current in a metallic system. Further, the interaction of the magnetic field with different defects can lead to crystalline magnetic anisotropy, magnetovolume effects and a difference in the electromagnetic state between the grain boundary and the grain interior [76]. Therefore examination of the electronic structure can elucidate the underlying mechanisms associated with premature flux penetration at the defects. Electronic density of states and Bader charge analysis were performed using VASP to study the electronic structure of different defects in their equilibrium condition before and after the external magnetic field was applied.

TABLE II. Number of atoms in the simulation cell and the k-point mesh used for different grain boundaries.

Grain boundary	Atoms	k-point mesh
$\Sigma5$ (210)	60	$6 \times 1 \times 14$
$\Sigma5$ (310)	84	$4 \times 1 \times 14$
$\Sigma13$ (023)	104	$4 \times 1 \times 14$
$\Sigma37$ (016)	144	$4 \times 1 \times 9$
$\Sigma17$ (014)	68	$2 \times 1 \times 9$
$\Sigma3$ (111)	66	$4 \times 1 \times 7$
$\Sigma1$ (101)	72	$6 \times 1 \times 14$

A. Density of states (DOS)

Figure 5 shows the electronic density of states for bcc niobium, niobium with dislocation dipole structure and niobium bicrystals with symmetric tilt grain boundaries. The DOS curve below the Fermi level (0 eV) represents the occupied states and the curve above the Fermi level represents the unoccupied states [77,78]. All the electronic density of states calculations were performed using the tetrahedron smearing method with Blöchl corrections within the DFT framework [79]. The orbital decomposed DOS curves of bcc niobium show d-orbital splitting into two irreducible collective orbital representations t_{2g} and e_g [Fig. 5(a)]. The occupied t_{2g} bands (d_{xy}, d_{yz}, and d_{zx}) sit lower in energy than the e_g orbital ($d_{x^2-y^2}$ and d_{z^2}), while the opposite is true in the unoccupied states, as is expected for octahedral coordinated centers and reported in literature [15,80,81]. In contrast to a perfect niobium crystal, the degeneracy of t_{2g} and e_g states is lifted in the presence of defects such as dislocations and grain boundaries. The redistribution of the occupied states and an upward shift of the average energy in the DOS curve of $Nb_{15}Vac_1$ indicates a reduction in bond strength around the point defect thus decreasing the structural and electronic stability of niobium with a vacancy as compared to bcc niobium [Fig. 5(b)].

In the presence of dislocation dipole structures, the d state energies re-order to new iso-energetic d_{xy} and $d_{x^2-y^2}$ states, d_{yz} and d_{zx} states, and a nondegenerate d_{z^2} state [Fig. 5(c)]. The total DOS curve for niobium with a dislocation dipole structure is in good agreement with the previously reported DOS curve in literature [58]. Further, in the case of the $\Sigma5$ (310) symmetric tilt grain boundary, the degeneracy of e_g states is further lifted between the $d_{x^2-y^2}$ and d_{z^2} states [Fig. 5(e)]. Additionally, the initial degeneracy of t_{2g} states is reduced since only d_{yz} and d_{zx} states overlap with each other while d_{xy} is nondegenerate. Similar nondegenerate splitting of d states is observed in other grain boundaries; however, the extent

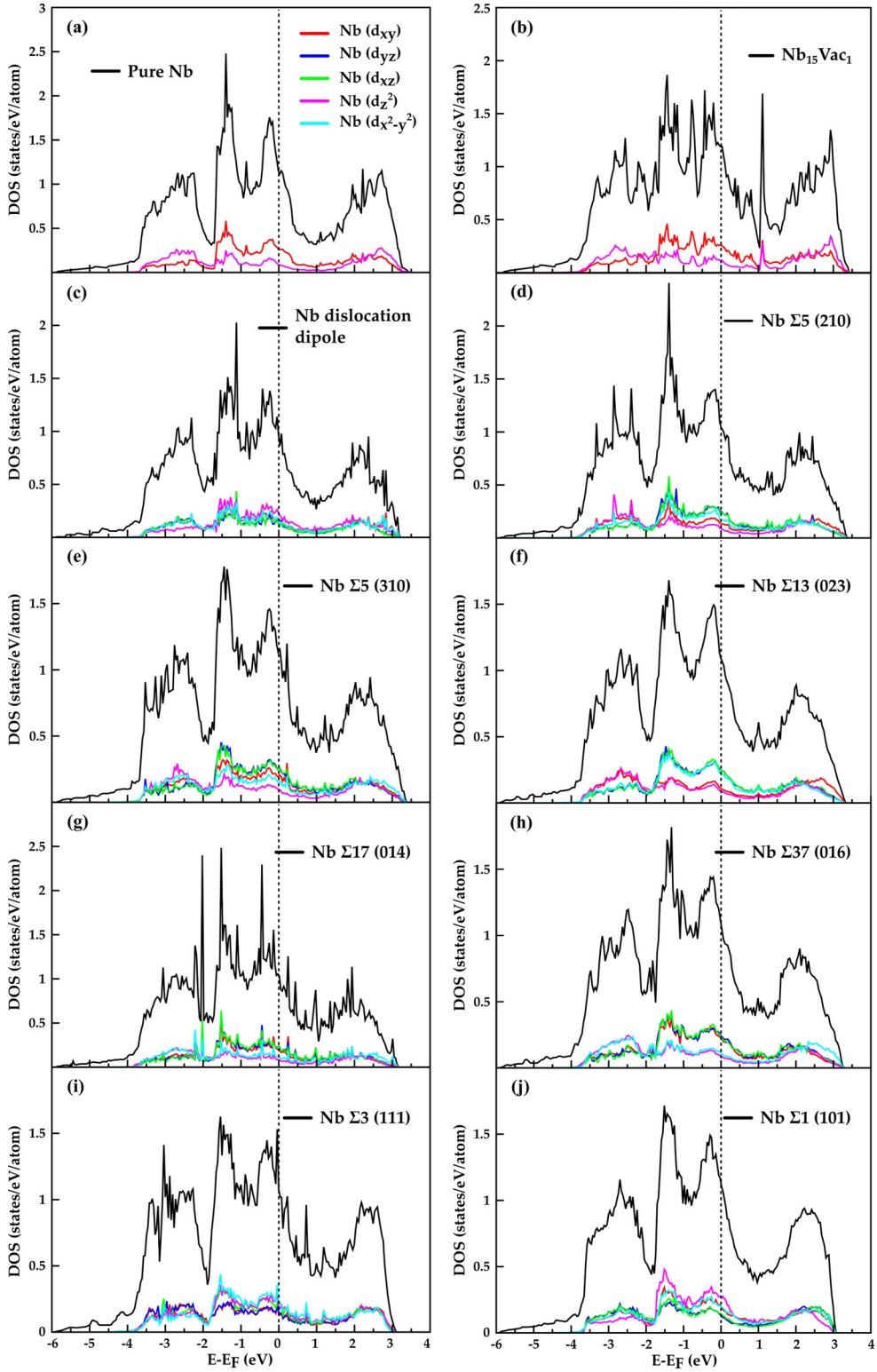

FIG. 5. Total (black) and orbital decomposed density of states curves (colored curves) for (a) bcc niobium, (b) niobium with 6.25 at% of vacancy, (c) screw dislocation dipole, [(d)−(h)] ⟨100⟩ family of STGBs, (i) ⟨110⟩ family of STGB, and (j) ⟨111⟩ family of STGB.

of nondegeneracy is different in different grain boundaries [Figs. 5(d)–5(j)]. Thus the degeneracy of the valence and conduction band *d* states is removed due to the localized bonding distortion at the defects. The partial or complete removal of the *d* state degeneracy is determined by the extent and nature of asymmetry introduced by the defect [82].

B. Bader charge analysis

The response of a material to an external source depends on the nature of atomic bonding between the atoms associated with the atomic charge distribution [83,84]. The charge obtained from the first-principles calculations was separated

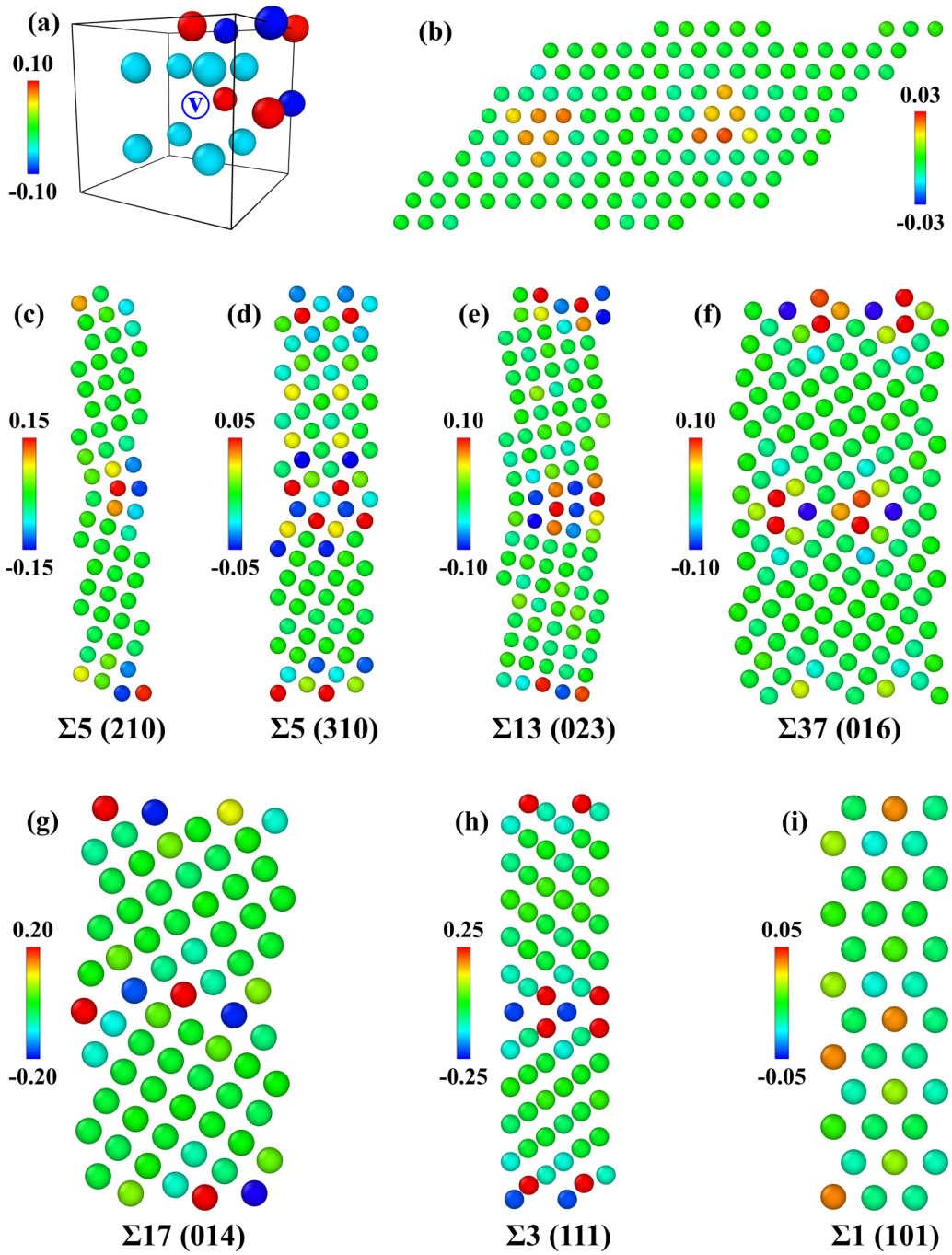

FIG. 6. Bader charge analysis for (a) bcc niobium with 6.25 at% of vacancy, (b) screw dislocation dipole, (c)–(g) ⟨100⟩ family of STGBs, (h) ⟨110⟩ family, and (i) ⟨111⟩ family of STGB. The atoms are colored according to the Bader charge on each atom.

and determined for each atom using the Bader charge analysis [85,86]. An expanded semi-core pseudopotential was used in this case to ensure proper assignment of electron density to individual nuclei. Figure 6 shows the Bader charges on the atoms around different defects. A significant amount of charge accumulation (0.1 e) and depletion (−0.1 e) was observed in niobium with 6.25 at% vacancy as a result of decreased atomic coordination number which leads to reduced hybridization between the electrons [Fig. 6(a)]. Charge redistribution around the dislocation dipole core structures is considerably lower (±0.03) due to the symmetric nature of the line defect [Fig. 6(b)]. Considerable charge redistribution varying from 0.05 e to 0.25 e was observed in the bi-crystals especially around the grain boundary atoms [Figs. 6(c)–6(i)]. For example, for the Σ13 (023) STGB some of the grain boundary atoms gained s Bader charge of 0.12 e (red atoms) while some GB atoms have Bader charge of −0.10 e (blue atoms) as compared to the Nb atoms away from the GB which have 0.0 Bader charge (green atoms, which are the same as perfect bcc Nb). Thus, valence charge transfer around the defects leads to localization of electrons, and their significantly different magnetic properties as compared to the bulk. This in turn enhances the tendency of niobium towards magnetism in the presence of external magnetic field.

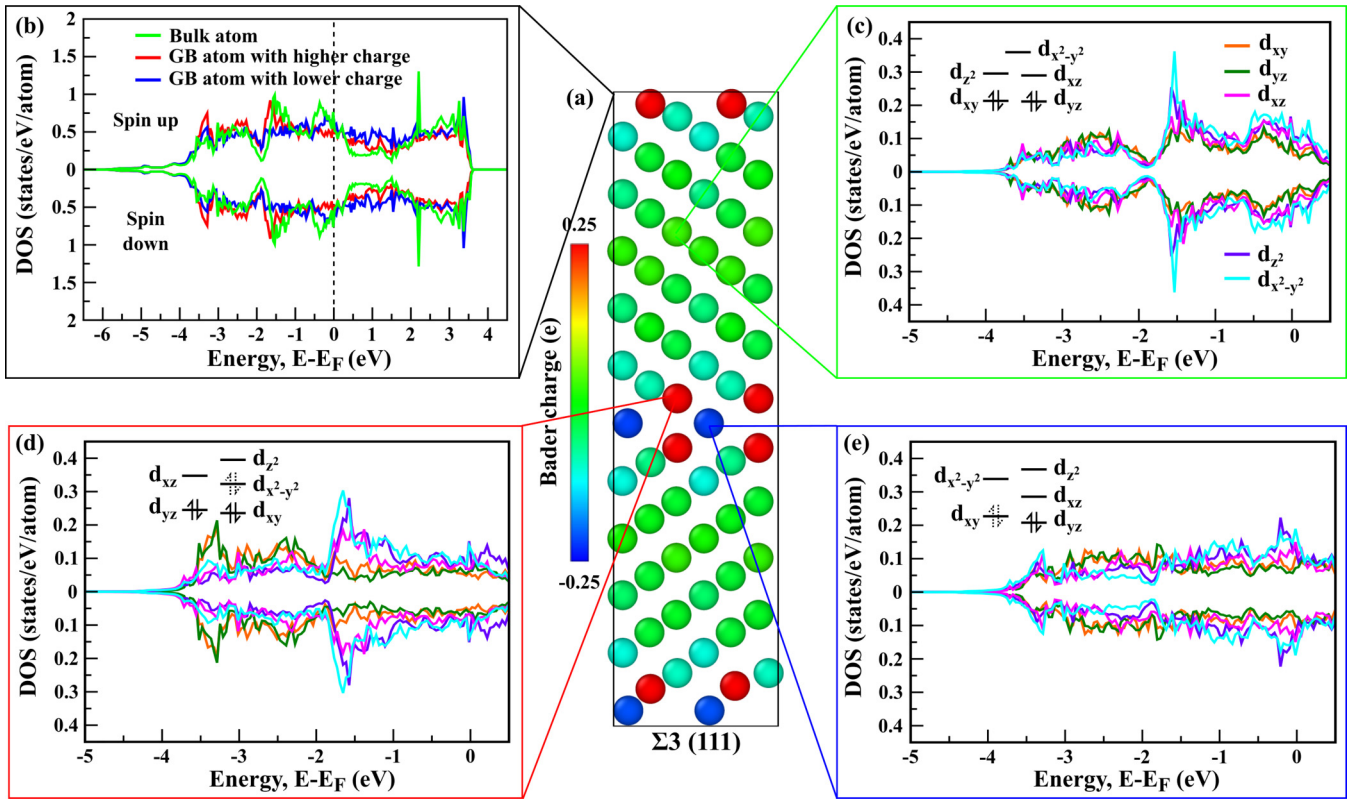

FIG. 7. (a) Bader charge analysis for Σ3 (111) STGB in niobium. Atoms are colored according to the Bader charge on each atom. (b) Partial DOS curves for different atoms selected based on Bader charge analysis of the Σ3 (111) STGB. Orbital decomposed DOS curves for bulk atoms (c), grain boundary atoms with charge accumulation (d) and depletion (e), respectively, below the Fermi level. Note that the upward moving DOS are spin up and downward are spin down.

The partial and orbital decomposed DOS for different atoms of all the grain boundaries studied were obtained to determine the localized effect of planar defects on retained flux density. As an illustration, the orbital and partial DOS are shown for the Bader atoms of Σ3 (111) GB, the grain boundary with highest magnetic moment and residual flux density (Fig. 7). The Σ3 (111) GB in Fig. 7(a) is colored based on the Bader charge analysis, where green atoms (0.0 e) represent the bulk niobium atoms away from the GB and the red (0.25 e) and blue atoms (−0.25 e) represent the GB atoms with accumulated and depleted charge respectively. The partial DOS for the niobium atoms far from the GB (green), and near the grain boundary (red and blue) with accumulated and depleted charge respectively are different from each other [Fig. 7(b)]. In bulk Nb atoms, localization of d orbitals was observed due to $d_{x^2-y^2}$ and d_{z^2} around −1.5 eV [Fig. 7(c)]. In red atoms [Fig. 7(d)], the accumulated electrons occupy $d_{x^2-y^2}$ orbitals in addition to d_{yz} and d_{xy} orbitals already occupied by the original 4d electrons. However, a stronger localization of d orbitals was observed in the grain boundary atoms with accumulated Bader charge from the additional peaks of d_{yz} and d_{zx} orbitals around −3.5 eV [Fig. 7(d)]. In blue atoms [Fig. 7(e)], the delocalization contribution is apparent in the smoother DOS curve of the GB atoms with depleted Bader charge. The spin-up and spin-down DOS curves are symmetric for the grain boundary atoms as well as for the atoms away from grain boundary and there is no net magnetic moment in the bicrystal simulation cell. However, the accumulation and depletion of charge at the grain boundary atoms can enhance nonparamagnetism in niobium, leading to a magnetized state when the material is exposed to an external magnetic field. Such nonparamagnetic behavior has been observed in niobium where the material underwent transition from a nonmagnetic state to a low-spin antiferromagnetic state to a high-spin ferromagnetic state upon lattice expansion [87,88].

V. SUMMARY

In summary, the present work provides a theoretical point of view to understand the interaction of an external magnetic field with lattice defects such as dislocations and grain boundaries and its effect on the magnetic properties of niobium via first-principles methods. Equilibrium defect structures were obtained using DFT methods and the external magnetic field was applied within the FP-LAPW code formulation. The magnitude of residual field at a vacancy was found to be significantly smaller than a dislocation dipole and grain boundaries, with grain boundary character playing a significant role. Further, the electronic structure of defects was determined using density of states and Bader charge analysis within first-principles framework to examine the underlying mechanism of interactions between external magnetic field and defects. Charge redistribution and splitting of d states in the defect region suggest significantly different magnetic properties and nonparamagnetic behavior as compared to bcc niobium. The different electronic structure of defects as compared to bulk

niobium indicates a magnetized state in the presence of an external magnetic field that thereby promotes early flux penetration at defects. This work suggests that flux pinning at defects can take place either via electron-scattering mechanism or due to crystal anisotropy or both mechanisms simultaneously.

ACKNOWLEDGMENTS

This work was supported by the US Department of Energy (Awards No. DE-SC0009962 and No. DE-SC0009960). We thank Peter Lee and Shreyas Balachandran from the National High Magnetic Field Laboratory, Florida State University for many helpful suggestions and discussions. Additionally, PG and KNS acknowledge Research Computing at Arizona State University for providing high performance computing resources that have contributed to the research results reported in this paper. In addition, we would like to thank Ilaksh Adlakha (Arizona State University) for the initial dislocation core structure.

[1] B. Glowacki, X.-Y. Yan, D. Fray, G. Chen, M. Majoros, and Y. Shi, Phys. C Supercond. **372**, 1315 (2002).
[2] J. L. H. Lindenhovius, E. M. Hornsveld, A. den Ouden, W. A. J. Wessel, and H. H. J. ten Kate, IEEE Trans. Appl. Supercond. **10**, 975 (2000).
[3] P. Dhakal, G. Ciovati, and G. R. Myneni, Phys. Rev. Accel. Beams **20**, 032003 (2017).
[4] P. Garg, S. Balachandran, I. Adlakha, P. J. Lee, T. R. Bieler, and K. N. Solanki, Supercond. Sci. Technol. **31**, 115007 (2018).
[5] E. E. Mitchell and S. K. H. Lam, Phys. Procedia **36**, 382 (2012).
[6] W. Wernsdorfer, Supercond. Sci. Technol. **22**, 064013 (2009).
[7] Z. Wang, S. Miki, and M. Fujiwara, IEEE J. Sel. Top. Quantum Electron. **15**, 1741 (2009).
[8] W. Meissner and R. Ochsenfeld, Naturwissenschaften **21**, 787 (1933).
[9] J. Knobloch and H. Padamsee, in *Proceedings of the 1997 Workshop on RF Superconductivity, Abano Terme, Padova* (INFN, Italy, 1997), p. 337.
[10] C. Vallet, M. Boloré, B. Bonin, J. Charrier, B. Daillant, J. Gratadour, F. Koechlin, and H. Safa, in *Proceedings of the Third European Particle Accelerator Conference* (Frontières, Gif-sur-Yvette, 1992), Vol. 2, p.1295.
[11] S. Aull, O. Kugeler, and J. Knobloch, Phys. Rev. Spec. Top. - Accel. Beams **15**, 062001 (2012).
[12] F. Peter, M. Muck, and C. Heiden, IEEE Trans. Appl. Supercond. **3**, 2968 (1993).
[13] A. Wildes, J. Mayer, and K. Theis-Bröhl, Thin Solid Films **401**, 7 (2001).
[14] P. Dhakal, G. Ciovati, P. Kneisel, and G. R. Myneni, IEEE Trans. Appl. Supercond. **25**, 1 (2015).
[15] P. Garg, I. Adlakha, S. Balachandran, T. Bieler, P. Lee, and K. Solanki, in *Proceedings of International Conference on RF Superconductivity (SRF'17)* (JACOW, Geneva, Switzerland, 2018), pp.741–745.
[16] A. Gurevich, Rev. Accel. Sci. Technol. **5**, 119 (2012).
[17] A Grassellino and A Romanenko and D Sergatskov and O Melnychuk and Y Trenikhina and A Crawford and A Rowe and M Wong and T Khabiboulline, and F Barkov, Supercond. Sci. Technol. **26**, 102001 (2013).
[18] T. Kubo, Prog. Theor. Exp. Phys. **2016**, 053G01 (2016).
[19] A. Gurevich and G. Ciovati, Phys. Rev. B **87**, 054502 (2013).
[20] P. Dhakal, G. Ciovati, and G. R. Myneni, Conf. Proc. C **1205201**, 2426 (2012).
[21] S. Huang, T. Kubo, and R. Geng, Phys. Rev. Accel. Beams **19**, 082001 (2016).
[22] C. Benvenuti, S. Calatroni, I. E. Campisi, P. Darriulat, M. A. Peck, R. Russo, and A.-M. Valente, Phys. C Supercond. **316**, 153 (1999).
[23] D. C. Ford, L. D. Cooley, and D. N. Seidman, Supercond. Sci. Technol. **26**, 095002 (2013).
[24] J. Knobloch, in *Hydrogen in Materials and Vacuum Systems: First International Workshop on Hydrogen in Materials and Vacuum Systems*, edited by G. R. Myneni and S. Chattopadhyay, AIP Conf. Proc No. 671 (AIP, New York, 2003), pp.133–150.
[25] P. Dhakal, G. Ciovati, G. Myneni, K. Gray, N. Groll, P. Maheshwari, D. McRae, R. Pike, T. Proslier, and F. Stevie, Phys. Rev. Spec. Top.-Accel. Beams **16**, 042001 (2013).
[26] P. J. Lee, A. A. Polyanskii, A. Gurevich, A. A. Squitieri, D. C. Larbalestier, P. C. Bauer, C. Boffo, and H. T. Edwards, Phys. C: Supercond. **441**, 126 (2006).
[27] K. Gifkins, C. Malseed, and W. Rachinger, Scr. Metall. **2**, 141 (1968).
[28] A. DasGupta, C. Koch, D. Kroeger, and Y. Chou, Philos. Mag. B **38**, 367 (1978).
[29] B. Khanra, Phys. Status Solidi B **72**, 303 (1975).
[30] B. Cai, Y. Chou, and A. D. Gupta, Philos. Mag. B **55**, 55 (1987).
[31] C. Z. Antoine, Phys. Rev. Accel. Beams **22**, 034801 (2019).
[32] G. Ciovati, P. Kneisel, G. Myneni, G. R. Myneni, G. R. Myneni, and S. Chattopadhyay, *Performances of High Purity Niobium Cavities with Different Grain Sizes* (Thomas Jefferson National Accelerator Facility, Newport News, VA, 2006).
[33] G. Ciovati, P. Kneisel, and A. Gurevich, Phys. Rev. Spec. Top. - Accel. Beams **10**, 062002 (2007).
[34] Z.-H. Sung, P. J. Lee, A. Gurevich, and D. C. Larbalestier, Supercond. Sci. Technol. **31**, 045001 (2018).
[35] A. Gurevich and L. D. Cooley, Phys Rev B **50**, 13563 (1994).
[36] R. Wördenweber, A. Pruymboom, and P. H. Kes, J. Low Temp. Phys. **70**, 253 (1988).
[37] P. J. Lee, A. A. Polyanskii, Z. Sung, D. C. Larbalestier, C. Antoine, P.C. Bauer, C. Boffo, and H. T. Edwards, in *Single Crystal - Large Grain Niobium Technology: International Niobium Workshop*, edited by G. R. Myneni, T. Carneiro, and A. Hutton, AIP Conf. Proc. No. 927 (AIP, New York, 2007), p. 113.
[38] A. Narlikar and D. Dew-Hughes, Phys. Status Solidi B **6**, 383 (1964).
[39] Z.-H. Sung, M. Wang, A. A. Polyanskii, C. Santosh, S. Balachandran, C. Compton, D. C. Larbalestier, T. R. Bieler, and P. J. Lee, J. Appl. Phys. **121**, 193903 (2017).
[40] M. Wang, P. Lee, C. Compton, T. Bieler, S. Chetri, S. Balachandran, and A. Polyanskii, in *Proceedings of International Conference on RF Superconductivity (SRF'17)*, (JACOW, Geneva, Switzerland, 2018), p. 781.
[41] T. Matsushita, *Flux Pinning in Superconductors* (Springer, Berlin, 2007).

[42] H. Ullmaier, K. Papastaikoudis, S. Takacs, and W. Schilling, Phys. Status Solidi B **41**, 671 (1970).
[43] A. Campbell and J. Evetts, Adv. Phys. **21**, 199 (1972).
[44] L. Vinnikov, E. Zasavitskii, and S. Moskvin, Sov. Phys.-JETP **56**, 1288 (1982).
[45] C. Pande and M. Suenaga, Appl. Phys. Lett. **29**, 443 (1976).
[46] G. Kresse and J. Hafner, Phys. Rev. B **47**, 558 (1993).
[47] G. Kresse and J. Hafner, J. Phys. Condens. Matter **6**, 8245 (1994).
[48] G. Kresse and J. Furthmüller, Phys. Rev. B **54**, 11169 (1996).
[49] P. E. Blöchl, Phys. Rev. B **50**, 17953 (1994).
[50] H. J. Monkhorst and J. D. Pack, Phys Rev B **13**, 5188 (1976).
[51] G. Alefeld and J. Völkl, *Hydrogen in Metals I: Basic Properties*, Topics in Applied Physics Vol. 28 (Springer-Verlag, Berlin and New York, 1978).
[52] T. R. Mattsson and A. E. Mattsson, Phys. Rev. B **66**, 214110 (2002).
[53] C. Wolverton, Acta Mater. **55**, 5867 (2007).
[54] T. Korhonen, M. J. Puska, and R. M. Nieminen, Phys. Rev. B **51**, 9526 (1995).
[55] P.A. Korzhavyi, I. A. Abrikosov, B. Johansson, A. V. Ruban, and H. L. Skriver, Phys. Rev. B **59**, 11693 (1999).
[56] A. Stroh, Philos. Mag. **3**, 625 (1958).
[57] E. Clouet, L. Ventelon, and F. Willaime, Phys. Rev. Lett. **102**, 055502 (2009).
[58] L. Dezerald, L. Ventelon, E. Clouet, C. Denoual, D. Rodney, and F. Willaime, Phys. Rev. B **89**, 024104 (2014).
[59] S. Plimpton, J. Comput. Phys. **117**, 1 (1995).
[60] M. R. Fellinger, H. Park, and J. W. Wilkins, Phys. Rev. B **81**, 144119 (2010).
[61] J. D. Rittner and D. N. Seidman, Phys. Rev. B **54**, 6999 (1996).
[62] M. Rajagopalan, I. Adlakha, M. A. Tschopp, and K. N. Solanki, JOM **69**, 1398 (2017).
[63] I. Adlakha, M. A. Bhatia, M. A. Tschopp, and K. N. Solanki, Philos. Mag. **94**, 3445 (2014).
[64] M. Rajagopalan, M. A. Bhatia, M. A. Tschopp, D. J. Srolovitz, and K. N. Solanki, Acta Mater. **73**, 312 (2014).
[65] K. N. Solanki, M. A. Tschopp, M. A. Bhatia, and N. R. Rhodes, Metall. Mater. Trans. A **44**, 1365 (2013).
[66] M.A. Tschopp, K .N. Solanki, F. Gao, X. Sun, M. A. Khaleel, and M. F. Horstemeyer, Phys. Rev. B **85**, 064108 (2012).
[67] E. Wachowicz and A. Kiejna, Comput. Mater. Sci. **43**, 736 (2008).
[68] D. Singh and A. Parashar, Comput. Mater. Sci. **143**, 126 (2018).
[69] S. Sharma, J. K. Dewhurst, C. Ambrosch-Draxl, S. Kurth, N. Helbig, S. Pittalis, S. Shallcross, L. Nordström, and E. K. U. Gross, Phys. Rev. Lett. **98**, 196405 (2007).
[70] S. Sharma, S. Pittalis, S. Kurth, S. Shallcross, J. K. Dewhurst, and E. K. U. Gross, Phys. Rev. B **76**, 100401 (2007).
[71] H. Jin, O. D. Restrepo, N. Antolin, S. R. Boona, W. Windl, R. C. Myers, and J. P. Heremans, Nat Mater **14**, 601 (2015).
[72] J.-Y. Yang, S.-Y. Yue, and M. Hu, Phys. Rev. B **94**, 235153 (2016).
[73] Q. Du, V. Faber, and M. Gunzburger, SIAM Rev. **41**, 637 (1999).
[74] M. A. Bhatia, S. N. Mathaudhu, and K. N. Solanki, Acta Mater. **99**, 382 (2015).
[75] P. C. Millett, T. Desai, V. Yamakov, and D. Wolf, Acta Mater. **56**, 3688 (2008).
[76] T. Watanabe, S. Tsurekawa, X. Zhao, and L. Zuo, Scripta Materialia **54**, 969 (2006).
[77] P. Garg, I. Adlakha, and K. N. Solanki, Acta Mater. **153**, 327 (2018).
[78] P. Garg, M. A. Bhatia, S. N. Mathaudhu, and K. N. Solanki, in *Magnesium Technology 2017*, edited by K. N. Solanki, D. Orlov, A. Singh, and N. R. Neelameggham (Springer, Berlin, 2017), pp. 483–489.
[79] P. E. Blöchl, O. Jepsen, and O. K. Andersen, Phys. Rev. B **49**, 16223 (1994).
[80] D. C. Ford, P. Zapol, and L. D. Cooley, J. Phys. Chem. C **119**, 14728 (2015).
[81] G. B. Grad, P. Blaha, J. Luitz, K. Schwarz, A. Fernández Guillermet, and S. J. Sferco, Phys. Rev. B **62**, 12743 (2000).
[82] G. Lucovsky, C. C. Fulton, Y. Zhang, Y. Zou, J. Luning, L. F. Edge, J. L. Whitten, R. J. Nemanich, H. Ade, D. G. Schlom, V. V. Afanase'v, A. Stesmans, S. Zollner, D. Triyoso, and B. R. Rogers, IEEE Trans. Device Mater. Reliab. **5**, 65 (2005).
[83] P. Garg, M.A. Bhatia, and K. N. Solanki, J. Alloys Compd. **788**, 413 (2019).
[84] P. Garg, I. Adlakha, and K. N. Solanki, in *Magnesium Technology 2019*, edited by V. V. Joshi, J. B. Jordon, D. Orlov, and N. R. Neelameggham (Springer, Berlin, 2019), pp. 231–237.
[85] E. Sanville, S.D. Kenny, R. Smith, and G. Henkelman, J. Comput. Chem. **28**, 899 (2007).
[86] D. Carballo-Córdova, M. Ochoa-Lara, S. Olive-Méndez, and F. Espinosa-Magaña, Philos. Mag. **99**, 181 (2019).
[87] A. R. Jani, N. E. Brener, and J. Callaway, Phys. Rev. B **38**, 9425 (1988).
[88] V. L. Moruzzi and P. M. Marcus, Phys. Rev. B **42**, 10322 (1990).